THE JOURNAL OF PHYSICAL CHEMISTRY C

Article

pubs.acs.org/JPCC

Electrical Characterization of 4-Mercaptophenylamine-Capped Nanoparticles in a Heterometallic Nanoelectrode Gap

Ninet Babajani,[†] Peter Kowalzik,[†] Rainer Waser,[†] Melanie Homberger,[‡] Corinna Kaulen,[‡] Ulrich Simon,[‡] and Silvia Karthäuser*,[†]

[†]Peter Grünberg Institut (PGI-7) and JARA−Fundamentals of Future Information Technologies, Forschungszentrum Jülich GmbH, D-52425 Jülich, Germany

[‡]Institute of Inorganic Chemistry and JARA−Fundamentals of Future Information Technologies, RWTH Aachen University, D-52074 Aachen, Germany

Supporting Information

ABSTRACT: One concept to build up hybrid electronic devices based on molecules or nanoparticles with rectifying properties is based on nanoscale objects that are immobilized between two electrodes composed of different metals forming asymmetric contacts. Following this concept, we introduce an optimized procedure to fabricate heterometallic nanoelectrodes with a separation of only 5 nm. Gold nanoparticles (AuNPs) with a diameter of 15 nm, stabilized with 4-mercaptophenylamine, were used to form electrode1-molecule/AuNP/molecule-electrode2 devices comprising at most a small number of AuNPs. Immobilization was performed by dielectrophoretic trapping. The molecular properties of 4-mercaptophenylamine are reflected in transition voltage spectroscopy features of the device. Cyclic current−voltage measurements on 20 functional devices revealed distinct differences in conductivities based on minor differences in device geometry. Analysis of the electron transport characteristics discloses that under these experimental conditions an asymmetric contact configuration alone is not sufficient for building up a molecule-based rectifier.

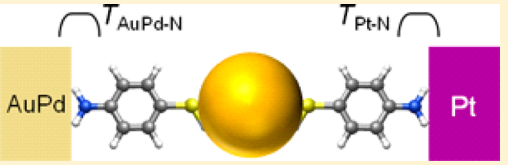

INTRODUCTION

Hybrid device technologies based on molecules or nanoparticles or, more general, nanoscale objects are considered to supplement silicon-based nanoelectronic approaches when miniaturization limits are reached. Following the concept of integrating molecular electronic devices into traditional CMOS circuitry nanoelements with tailored functionalities are employed to increase integration density.[1] In this context, one major challenge is to fabricate nanodevices bearing rectifier functionality in a reliable way. In principle, two approaches can be applied in order to establish the functionality of a rectifier. One approach is to immobilize a nanoscale object with intrinsic rectifier properties between homometallic nanoelectrodes, like proposed by Aviram and Ratner[2] for molecules. However, using this approach, immobilization occurs in a nondirectional manner, and thus the forward direction of the diode cannot be predefined. A second concept to construct a rectifier is to immobilize isotropic nanoelements between different nanoelectodes, i.e., in a heterometallic nanogap, and, thus, to construct asymmetric contacts.[3−5] Hence, unequal work functions of the metals or different transmission coefficients between the molecular anchor groups and the electrodes result in the formation of a rectifier. The latter approach should become feasible, if the two electrodes building the nanogap are fabricated from different metals, i.e., possess significant different work functions and are separated by a few nanometers only.

Several electronic testbeds exist in the laboratory which can be used to connect nanoscale objects to two electrodes composed of different metals, such as scanning probe methods,[6] hanging mercury drop junctions,[7] nanopore devices,[8] crossed wire junctions,[9] on-wire lithography techniques,[10] electroplating,[11] or junctions with top electrodes defined by nanotransfer printing.[12] However, these methods are not adjustable to CMOS fabrication technology. Lithographically fabricated metallic nanoelectrodes may be the most suited approach to realize this type of device.[13,14] Recently, we introduced a fabrication route for homometallic nanoelectrodes with a separation of only 3 nm utilizing e-beam lithography.[15] In this context, we demonstrated that the final limits of patterning accuracy derive from proximity effects. We succeeded in minimizing these proximity effects to a large extent by a nanoelectrode pattern design based on simulations involving the proximity effect-related exposure dose. Applying this optimized e-beam lithography process, we were able to fabricate nanoelectrodes bearing separations of only 3 nm in a highly reproducible manner.

However, if a rectifier function shall be approached, heterometallic nanogaps are needed. To this end, approaches for fabricating heterometallic nanogaps involve the electrodeposition of a second metal on a lithographically preformed electrode,[16,17] a molecular lithography technique,[18] or a self-alignment procedure.[19] Here, we introduce a highly reprodu-

Received: June 17, 2013
Revised: September 16, 2013

   dx.doi.org/10.1021/jp405990y | J. Phys. Chem. C XXXX, XXX, XXX−XXX

cible process for the fabrication of a pair of heterometallic nanoelectrodes combining an optimized e-beam lithography process[15] with a self-alignment procedure[19] to form heterometallic nanogaps as small as 5 nm. To study the effects that arise from the different metals, gold nanoparticles (AuNPs) capped with mercaptophenylamine (MPA) have been synthesized and immobilized in the nanogap. The resulting asymmetric "electrode1-molecule/AuNP/molecule-electrode2" devices were characterized by cyclic electron transport measurements, transition voltage spectroscopy (TVS),[20−22] and scanning electron microscopy (SEM). We will show that devices resulting from immobilization of MPA-AuNPs in hetereometallic nanogaps reveal different transport characteristics depending on small differences in the device geometry. Hence, an asymmetric contact configuration alone is not a sufficient requirement for building up a molecule-based rectifier under these conditions.

EXPERIMENTAL METHODS

Chip Design. The heterometallic nanoelectrodes were deposited on a 1 × 1 in.^{2} silicon wafer covered with a 300 nm insulating silicon oxide layer. This chip was cut into 3 × 3 samples with dimensions of 6 × 6 mm^2 each (see Figure 1). On each sample nine nanoelectrode arrays with six heterometallic nanogaps were fabricated by electron beam lithography (EBL) in a lift-off process. The size of the nanogaps formed in between the central Pt electrode (thickness 13 nm) and the peripheric AuPd electrodes (thickness 10 nm) can be tuned between 5 and 20 ± 2 nm according to the size of the nanoelement which is supposed to be contacted.

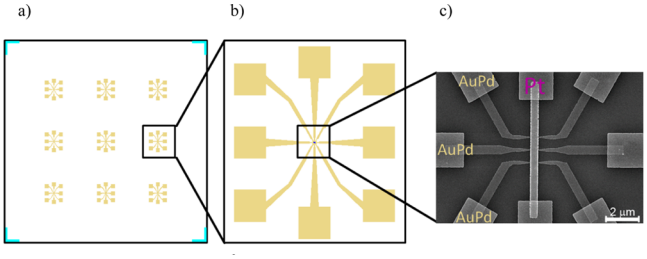

Figure 1. (a) Layout of a 6 × 6 mm^2 Si/SiO_2 sample. (b) Magnified section displaying one array comprising six heterometallic nanogaps, formed between the central Pt electrode and the peripheric AuPd electrodes (contact pad size: 100 × 100 μm^2; AuPd). (c) SEM image of the inner part of one nanogap array showing the six heterometallic nanogaps.

Fabrication of Heterometallic Nanogaps. The first step in the fabrication of the heterometallic nanogaps was the definition of the platinum electrodes by EBL in a lift-off process. The previously optimized double-layer resist stack[15] (Figure 2) was employed also in this case. The undercut layer, PMGI (1% polymethylglutarimide in cyclopentanone, micro resist technology GmbH), was spin-coated with a speed of 4000 rpm for 60 s (thickness 45 nm), baked on a hot plate at 250 °C for 7 min, and preexposed for 1 min with UV light (320 nm). Next, the structure defining resist, PMMA (1% poly(methyl methacrylate) in ethyl lactate, molecular weight 950K, AR-P 679.02, Allresist GmbH), was spin-coated with 2000 rpm for 60 s (thickness 25 nm) and baked at 180 °C for 7 min.

The nanoelectrode structures were written by EBL with the Gaussian vector scan system EBPG 5000+ (Vistec Electron Beam GmbH) applying an acceleration voltage of 50 kV. The pattern for the Pt-electrodes were written with a dose of 390 μC cm^{-2}, a beam current of 5 nA, and a beam step size of d_s = 10 nm. The exposed areas of PMMA 950K were removed by development in an isopropanol/H_2O (7:3) mixture for 100 s, and the development was stopped by rinsing the sample with demineralized water for 30 s. Next, PMGI was developed by immersing the sample into the developer MF-21A (MicroChem) for 40 s. This second development procedure was stopped by rinsing the sample with demineralized water for 60 s and blowing dry with nitrogen. Because of this procedure, using a double-layer resist stack and a two-step development process, the undercut in the PMGI layer can be controlled (Figure 2).

The Pt electrodes were deposited by an e-gun-evaporator at the pressure of $p < 1 \times 10^{-7}$ mbar. The metallization step started with a 1 nm thin titanium adhesion layer (deposition rate 0.05 nm/s) and proceeded with a 13 nm Pt layer (deposition rate 0.3 nm/s). Subsequently, an 11 nm Al layer was evaporated on top of the Pt electrode with the same deposition rate. After the metallization process, the sample was exposed to air whereby the aluminum was oxidized. Thus, an augmented Al_2O_3 layer on top of the Pt layer with an overhang of about 13 ± 2 nm was formed for the following self-alignment process. The size of the overhang can be controlled by the thickness of the Al_2O_3 layer. After lift-off (warm acetone, 1.5 h) the predefined Pt electrodes (rms = 1 nm) with a width of 400 nm and a length of 6 μm with the Al_2O_3 hard mask on top remain.

The same double-layer resist stack and development procedure as described above for the definition of the Pt electrodes was applied to fabricate the AuPd nanoelectrodes. In the EBL step the parameters were adopted to the smaller width (20−500 nm) of the AuPd nanoelectrodes (exposure dose 400 μC/cm^{-2}, beam current 100 pA, beam step size 1.25 nm). After development a Ti adhesion layer (1 nm) and a 10 nm AuPd layer were evaporated with a deposition rate of 0.2 nm/s followed by lift-off. As a result of this process, AuPd nanoelectrodes were defined (Figure 3). The separation

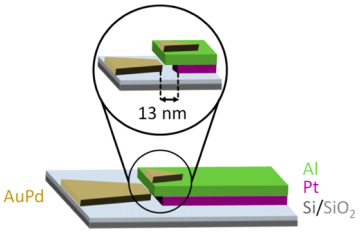

Figure 3. Schematic of the self-alignment step using the Al_2O_3 hard mask to form the gap between the central Pt and the AuPd electrodes.

Figure 2. Illustration of the process steps used for patterning nanoelectrodes by EBL with SiO_2 (300 nm; gray), PMGI (45 nm, blue), PMMA 950 K (25 nm, yellow), and platinum (13 nm, violet).

dx.doi.org/10.1021/jp405990y | J. Phys. Chem. C XXXX, XXX, XXX−XXX

between the Pt and the AuPd electrodes corresponds to the nanometer sized gap predefined by the Al_2O_3 hard mask on top of the Pt electrodes. Next, the Al_2O_3 layer was removed using the developer tetramethylammonium hydroxide (TMAH, AZ 326 MIF) in an ultrasonic bath. Subsequently, the wafer was washed in demineralized water for 2 min in isopropanol for 30 s and then blown dry with nitrogen. Finally, the contact pads (22 nm thickness, 100 × 100 μm^2) were patterned by optical lithography using a standard procedure.

Synthesis of 4-Mercaptophenylamine-Capped Gold Nanoparticles (MPA-AuNPs). MPA (4-mercaptophenylamine)-stabilized AuNPs were synthesized applying a solid phase supported approach, corresponding to the recently developed preparation protocol for aminooctanethiol (AOT)-capped AuNPs.[23] Thereby citrate-stabilized 15 nm AuNPs were immobilized on aminosilanized glass beads from aqueous solution (pH 5.5), acidified with HCl (0.1 M), and treated with an ethanolic solution of MPA in order to induce ligand exchange. Immobilization avoids aggregation of the partially protonated citrate-stabilized AuNPs upon acidification of the solution as well as electrostatically induced aggregation of the negatively charged citrate ligands and positively charged ammonium ligands, as described in the literature.[24] By ultrasonication MPA-AuNPs were released from the solid support, and ligand exchange was completed (Figure 4). Free

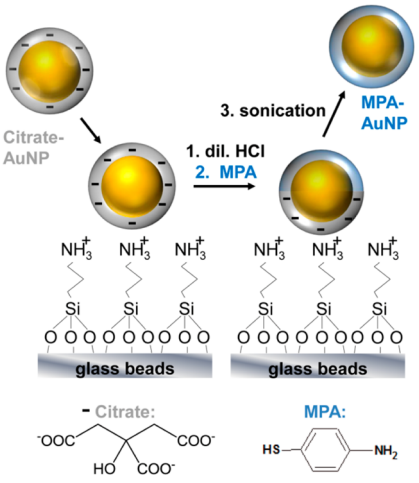

Figure 4. Preparation scheme of mercaptophenylamine (MPA)-capped AuNPs.

citrate molecules and excess of thiol ligands were removed by repeated centrifugation and redispersion in acidified water. In order to optimize dielectrophoretic trapping of the particles inside the nanogaps, the pH value, and thereby the degree of protonation, was systematically varied in HEPES buffer solution.

The synthesized MPA-AuNPs were characterized by electron microscopy (STEM, TEM) as well as by pH-dependent UV–vis spectroscopy, dynamic light scattering (DLS), and ζ-potential measurements.

Current–Voltage Measurements on MPA-AuNPs. MPA-AuNPs were immobilized in between heterometallic nanoelectrodes applying dielectrophoretic trapping (DEPT)[25,26] from a HEPES buffer solution at pH = 7.5 or at pH = 2. Successful trapping was achieved applying a dc electrical field (U_{dc} = 0.7–1 eV for t = 2 min) as described earlier.[27] Subsequently, electrical characterization was performed using a Keithley 6430 sub-femtoampere remote source meter at room temperature under vacuum.

SEM. Scanning electron microscopy images of the nanoelectrodes and the MPA-AuNP devices after electrical characterization were obtained with a SU8000 Series UHR Cold-Emission FE-SEM, at 10 kV acceleration voltage.

XPS. XPS measurements were performed using the PHI5000 VersaProbe II with monochromatic Al Kα radiation in large area mode (1.4 mm × 200 μm, 100 W, 20 kV). Survey scans as well as core level spectra of Pt 4f, Au 4f, O 1s, N 1s, and C 1s were recorded. Quantification of the survey scans was performed with the help of MULTIPAK Software.

RESULTS AND DISCUSSION

Heterometallic Nanogaps. Heterometallic nanoelectrodes with a separation of 5 ± 2 or 13 ± 2 nm, respectively, and a yield of over 50% were obtained applying the optimized fabrication process based on EBL and the self-alignment procedure, as described above. Figure 5 shows SEM images of a

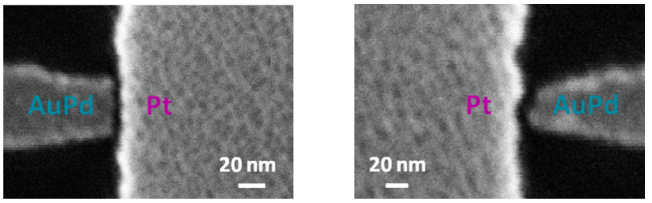

Figure 5. SEM image of a 5 nm gap (a) and a 13 nm gap (b) between an AuPd and a Pt electrode.

5 nm gap and a 13 nm gap between an AuPd and a Pt electrode. In this way, structural control over nanoelectrodes fabricated from different metals and forming heterometallic nanogaps was achieved with nanometer precision.

MPA-AuNPs. The TEM analysis (Figure 6) of the MPA-AuNPs synthesized according to our solid phase supported procedure reveals nanoparticles with a mean diameter of d = 15.2 ± 2.1 nm (based on 165 measured nanoparticles). The UV–vis spectra exhibit the typical plasmon peak for AuNPs. To demonstrate the degree of dispersion, we particularly monitored the spectral position of the plasmon peak maximum (λ_{max}), which is red-shifted upon particle agglomeration.

The amine group of the MPA ligand can be protonated or deprotonated depending on the pH of the surrounding solution. Therefore, we performed investigations concerning the pH-dependent agglomeration behavior of MPA-AuNPs. UV–vis and DLS measurements revealed that small agglomerates exist in solutions comprising a pH of 5, reflected by broadening of the plasmon peak maximum ranging from 500–580 nm (Table 1 and Table S1, see Supporting Information), although the positive ζ-potential of 24.3 ± 2.2 mV points to a positively charged ligand shell. A distinct UV–vis absorbance with λ_{max} = 528 nm observed for particles at pH = 3 indicates that nearly no agglomerates exist, corresponding to individual particles, most likely stabilized by electrostatic repulsion between the positively charged ligand shells. In order to immobilize single AuNPs in between the nanogaps, we concluded that the pH of the nanoparticle solution used for immobilization in the dielectrophoretic trapping experiments should be adjusted to values <3. In this regime individual or at least small agglomerates of AuNPs are present in solution and trapping of large agglomerates should be avoided. Comparing

dx.doi.org/10.1021/jp405990y | J. Phys. Chem. C XXXX, XXX, XXX–XXX

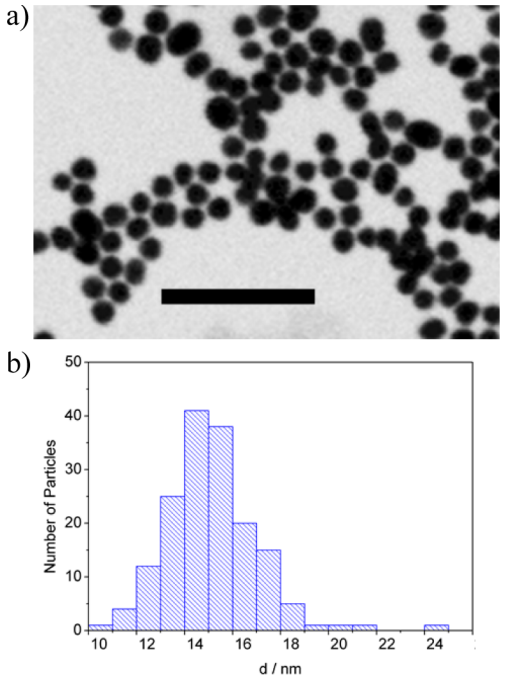

Figure 6. (a) SEM image (transmission mode, scale bar represents 100 nm) and (b) corresponding histogram of MPA-AuNPs deposited from ultrapure water at pH 5.5, revealing a mean diameter of 15.2 ± 2.1 nm.

Table 1. Analysis of MPA-AuNPs in Solution at pH 3 and 5, Including λ_{max} and fwhm determined from UV−vis Absorption Spectra, Hydrodynamic Diameter (D_h), and ζ-Potential, Evaluated from DLS Measurements

	pH 3	pH 5
λ_{max}/nm	528	529
fwhm/nm	60	75
D_h/nm	91	129
ζ-potential/mV	36.8 ± 3.5	24.3 ± 2.2

MPA-AuNP solutions at pH = 2 and at pH = 7.5, we found indeed that using solutions with a pH = 2 only small agglomerates or even a few single nanoparticles were trapped.

Transport Measurements. In order to prove the impact of asymmetric contacts of a molecule connected to two dissimilar electrodes, like in "nanoelectrode1-molecule-nanoelectrode2" devices,[5] cyclic I/U measurements were performed on MPA-capped AuNPs immobilized between a AuPd and a Pt nanoelectrode (Figure 7). Thus, dissimilar contacts between

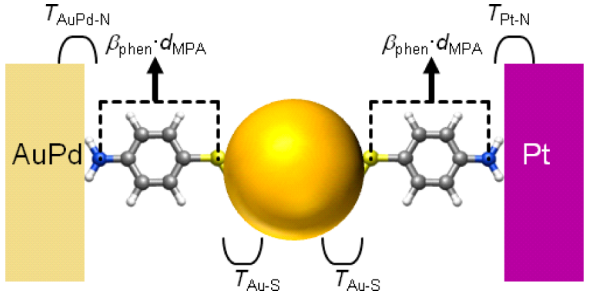

Figure 7. Schematic of "AuPd-MPA/AuNP/MPA-Pt" devices; the transmission coefficients between the respective molecular end groups and the metallic electrodes (T), the decay constant of phenylene (β_{phen}), and the molecular length of MPA (d_{MPA}) are indicated.

the amine-terminated MPA-AuNP and the respective nanoelectrode were formed. In this study we obtained 20 functional devices from 324 fabricated ones, i.e., from 324 trials to immobilize a MPA-AuNP by dielectrophoretic trapping between heterometallic nanogaps. Here, functional device means that more than 10 I/U curves were obtained in a reproducible manner, and the analysis of the measurements indicated molecular properties. The finally taken SEM images revealed in 10 cases a countable number or even very few MPA-AuNPs between the heterometallic nanoelectrodes. It should be noted that due to a strong influence of SEM imaging on the electronic properties of the device, these characterizations were done only after transport measurements. For all that, about 50% of the analyzed MPA-AuNP devices could be detached from the leads and transferred to the SEM without destroying the nanoelectrodes due to induced overvoltage.

The first obvious result of the transport investigations was that the conductivities of the 20 functional devices (for a source-drain voltage (U_{SD}) of 1 V) span a rather large range from 0.1 pS to 30 nS. However, a major number of MPA-AuNP devices (7 from 20) displayed conductivities at the upper limit of this conductivity range. Therefore, the devices were classified into two categories. Devices of category A (7 devices) exhibited a conductivity of 5−30 nS; i.e., these devices revealed large conductivities with only a small variance. On the other hand, devices of category B (13 devices) displayed conductivities in the range 2 nS−0.1 pS; i.e., in this category all other devices were merged. In Figures 8 and 9 sets of typical I/U measurements, Fowler−Nordheim plots, and SEM images for each category are shown (see also Supporting Information for another example of a category B device).

Comparing devices of categories A and B (Figures 8 and 9), it is quite evident that besides the I/U characteristics also the Fowler−Nordheim plots differ distinctively. Fowler−Nordheim plots are obtained from I/U data by plotting $\ln(I/U)$ vs $1/U$ (transition voltage spectroscopy (TVS)). According to Beebe,[20] the transition from direct to Fowler−Nordheim tunneling is indicated by a minimum in the Fowler−Nordheim plot. This minimum is denoted as transition voltage (U_{trans}) and is proportional to the tunneling barrier height (ϕ_B). Devices of category A exhibited noisy TVS curves without significant minimum in the measurement range from 0 to 1.7 V. Contrarily, MPA-AuNP devices of category B revealed low noise TVS curves with distinct minimum. From this minimum we deduced a tunneling barrier height of $\phi_{B,exp}$ = 0.85 ± 0.1 eV. This value is in good agreement with literature data for tunneling barrier heights corresponding to phenylene groups[29] ranging from 0.67 to 0.82 eV and confirms that the MPA molecules form the tunneling barrier in category B devices. On the other hand, the absence of a distinct minimum in the TVS curves of category A devices, i.e., devices with high conductivity, and the noisy I/U characteristic point to another transport mechanism.

The experimental I/U characteristics were further analyzed employing a fit routine based on the tunneling model of Simmons:[3,28]

$$I = \frac{eA}{2\pi h\bar{d}^2}\left\{\left(\overline{\Phi}_B - \frac{eU}{2}\right)\exp\left(-\frac{4\pi\bar{d}\sqrt{2m^*}}{h}\sqrt{\overline{\Phi}_B - \frac{eU}{2}}\right) - \left(\overline{\Phi}_B + \frac{eU}{2}\right)\exp\left(-\frac{4\pi\bar{d}\sqrt{2m^*}}{h}\sqrt{\overline{\Phi}_B + \frac{eU}{2}}\right)\right\} \quad (1)$$

dx.doi.org/10.1021/jp405990y | J. Phys. Chem. C XXXX, XXX, XXX−XXX

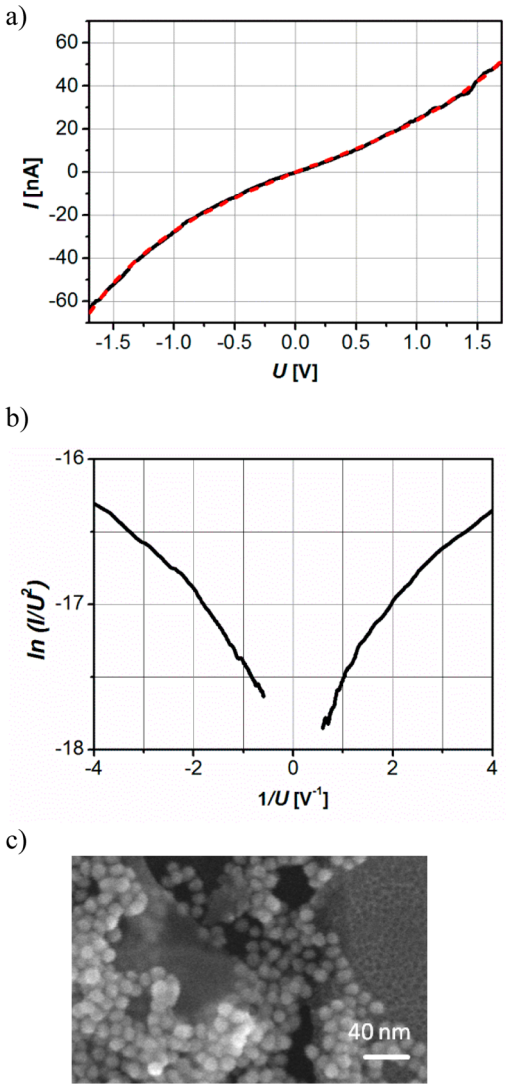

Figure 8. Representative measurements for MPA-AuNPs devices of category A: (a) I/U characteristic (black) and exponential fit according to the tunneling model[3,28] (dashed red). A positive voltage in the diagram corresponds to application of a positive bias voltage to the AuPd electrode, Pt electrode grounded. (b) Fowler–Nordheim plot. (c) SEM image.

with A = contact area, $\overline{\phi_B}$ = mean tunneling barrier height, $\overline{d}$ = mean tunneling distance, m^* = effective electron mass, and h = Planck's constant. Using this fitting procedure, detailed information on the formed devices like the mean tunneling barrier height and the mean tunneling distance were obtained. From these data the mean decay parameter $(\overline{\beta d})$ for devices of category A and B can be deduced using the transformation:

$$\overline{\beta} = \frac{4\pi}{h}\sqrt{2m^*\overline{\Phi_B}} \tag{2}$$

The mean decay parameter $(\overline{\beta d})$ for devices of category A and B obtained in this way are given in Table 2 together with the values for the mean tunneling distances. So far, it can be noted that both differ considerably, and the tunneling distance for devices of category A is about 0.5 nm smaller than the tunneling distance in devices of category B. This result is in accordance with the measured conductivities and the corresponding SEM images given in Figures 8 and 9. While the nanoelectrode gap in category A devices is bridged by an array of MPA-AuNPs and thus, a conduction pathway is likely built, only a few MPA-AuNPs are present in the gap of category B devices. It cannot be excluded from Figure 9d that there is a vacuum gap as small as 0.5 nm between the AuPd-electrode and the nearest MPA-AuNP.

In order to compare the mean decay parameter deduced from experimental I/U curves with theoretical values, we made a rough estimate of the tunneling current through a MPA-AuNP in contact with two electrodes using the single-channel Landauer formula for conductance (G_{mol}).[29−31] For this purpose we considered the geometry of our "AuPd-MPA/AuNP/MPA-Pt" devices (see Figure 7) in detail. Two tunneling barriers were formed by the molecular capping layer of the AuNP (between AuPd-electrode and MPA-AuNP, on one hand, and between MPA-AuNP and Pt-electrode, on the other). Furthermore, an additional tunneling barrier might be created in some devices by a vacuum gap remaining between the MPA-AuNP and one nanoelectrode resulting in a reduction of the conductivity. We observed this situation earlier in symmetrical BP3-AuNP devices.[32] However, for a first approximation, we calculated the tunneling current through our device without possible vacuum gap. The single-channel Landauer formula for conductance (G_{mol}) is given by[29−31]

$$G_{molecule} = \frac{I}{U} = G_0 \exp(-\beta d) T_L T_R \tag{3}$$

with G_0 = quantum of conductance, β = decay constant, d = molecular length, and $T_{L/R}$ = transmission coefficients for left metal–molecule and right metal–molecule contact. Applying this formula to our device geometry, i.e., two molecular junctions in series: "AuPd-MPA/AuNP/MPA-Pt", the following formula for conductance (G_{dev}) is derived:

$$1/G_{dev} = 1/G_{MPA1} + 1/G_{MPA2} \tag{4}$$

$$G_{dev} = (G_0 \exp(-\beta_{Phen} d_{MPA})) T_{Au\text{-}S} T_{AuPd-N} \times T_{Pt\text{-}N}(T_{AuPd\text{-}N} + T_{Pt\text{-}N})^{-1} \tag{5}$$

We employed the subsequent set of parameters: β_{Phen} = 4.6 nm^{-1},[33] d_{MPA} = 0.61 nm, $T_{Au\text{-}S}$ = 0.81,[29] $T_{AuPd\text{-}N} \sim T_{Au\text{-}N}$ = 0.19,[34] and $T_{Pt\text{-}N}$ = 0.29 deduced from the experimental single molecule conductance of diaminobenzene in contact with Pt electrodes given in Kiguchi et al.[35] Thus, the theoretical device conductance was obtained: 435 nS. This value is by a factor of about 10 higher than the measured conductivities of our MPA-AuNP devices of category A pointing to the fact that tunneling is a favorable transport mechanism in these devices. The smaller conductivities of the experimental devices of category A compared to the rough theoretical estimation can be explained by one of the following reasons. First of all, our parameter set is deduced from parameters or experimental values given in the literature, and an error limit of at least 20% should be considered for all β-values and transmission coefficients. Second, a small additional gap between the MPA-AuNPs and the electrodes may even remain in the devices of category A. A vacuum gap with a width of d_{vac} = 0.1–0.2 nm would already explain the difference between theoretical and measured device conductivities. This vacuum gap could be induced by a remaining positive charge of the MPA ligand shell after immobilization, leading to a repelling from one electrode. Third, if the assumed device geometry is not applicable and more than one nanoparticle is needed to bridge the gap

dx.doi.org/10.1021/jp405990y | J. Phys. Chem. C XXXX, XXX, XXX–XXX

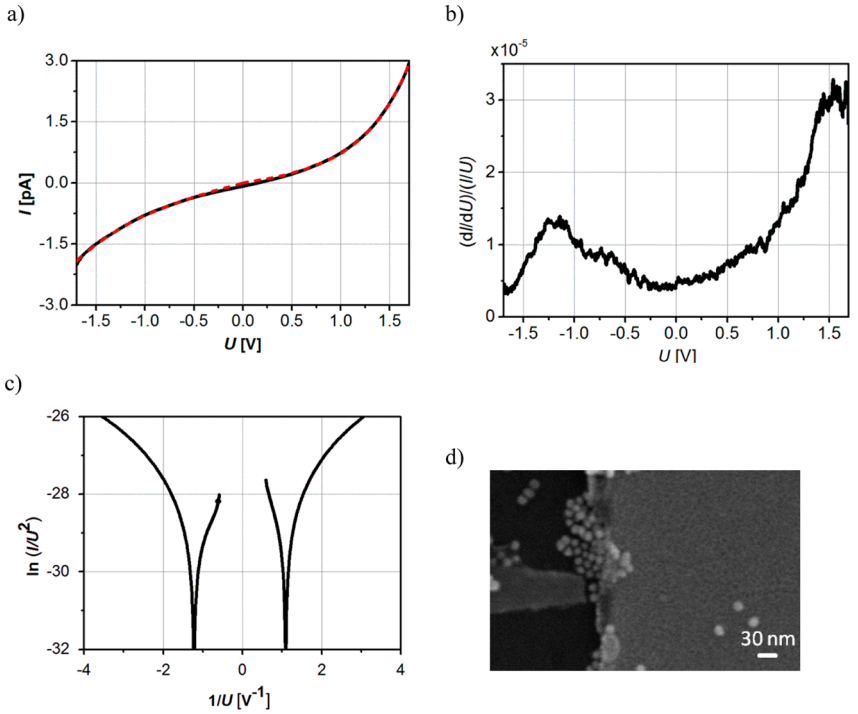

Figure 9. Representative measurements for MPA-AuNPs devices of category B: (a) cyclic I/U characteristic (black) and exponential fit according to the tunneling model[3,28] (dashed red). A positive voltage in the diagram corresponds to application of a positive bias voltage to the AuPd electrode. (b) Normalized differential conductivity calculated from the I/U data. (c) Fowler–Nordheim plot. (d) SEM image.

Table 2. Transport Parameter of MPA-AuNP Devices

	category A	category B
G_{exp} (U = 1 V)	5 nS–30 nS	0.1 pS–2 nS
$\phi_{B,exp}$		0.85 ± 0.1 eV
$\phi_{B,lit}$[29]	0.67–0.82 eV	
$(\overline{\beta d})$	10.2 ± 2	20.2 ± 2
$\overline{d}$	0.63 ± 0.1 nm	1.1 ± 0.2 nm
d_{vac}	0.15 ± 0.1 nm	0.65 ± 0.2 nm

between the nanoelectrodes, the conductivity of the device is further reduced.

However, the measurements of the device conductivity were reproducible; a part of the theoretical parameter set for the β values and transmission coefficients has been used successfully by us in other cases,[27,33] and the statistic points to a physical limit of the device conductivity of category A devices. In order to verify that the MPA ligand shell is still intact after immobilization, we performed XPS measurements of these MPA-AuNPs on Pt surfaces. XP spectra provide information on the relative quantity of the elements and the chemical identity of the organic compound. The obtained Pt 4f, Au 4f, N 1s, and C 1s core level spectra show peaks with binding energies corresponding to the adsorption of MPA on Au, as expected. However, the O 1s core level spectrum reveals an unexpected peak with a binding energy of 534.5 eV (see Figure S2). Since the examination of the C 1s core level shows no evidence of carbonyl or carboxyl formation, this peak was assigned to water molecules incorporated into the MPA ligand shell. The value of the O 1s binding energy can be attributed to electron-deficient oxygen involved in hydrogen bonds to amine groups.[36,37] Thus, water molecules linked to MPA by hydrogen bonds were identified.

Elemental quantification in terms of the atomic percentage ratio of carbon and oxygen was calculated from spectra by integration of the areas of C 1s and O 1s peaks after application of a Shirley background subtraction and correction for atomic sensitivity factors. The experimental carbon to oxygen ratio is 2.5 to 1, corresponding to a MPA to H_2O ratio of 1 to 2 taking the increasing attenuation of the C 1s photoelectrons by the thicker molecular overlayer into account. Furthermore, a small amount of chloride (Cl 2p) with an experimental carbon to chloride ratio of about 70 to 1 was obtained. These data reveal that the ligand shell of MPA-AuNPs includes besides MPA molecules also incorporated water molecules and chloride counterions. Based on these results, a detailed scheme of the ligand shell around the AuNPs with partly protonated amine groups, interlinked water molecules, and chloride ions is given in Figure 10.

The device conductivity for the enlarged capping layer ($G_{dev\text{-}large}$) applying the single-channel Landauer formula and including an additional shell of water molecules has been calculated, with d_{H_2O} = 0.24 nm (corresponding to the thickness of a shell of one water molecule including hydrogen bonds) and assuming $\beta_{H_2O} \sim \beta_{COOH}$ = 11.2 nm^{-1}, $T_{AuPd\text{-}H_2O} = T_{Pt-H_2O} \sim T_{Au\text{-}COOH}$ = 0.08.[29] The resulting $G_{dev\text{-}large}$ amounts to 10.1 nS. This value is in astonishing agreement with the measured device conductivity (5–30 nS), confirming that tunneling is the relevant transport mechanism in such devices. We like to point out that the roughly estimated $G_{dev\text{-}large}$, based on the device geometry schematically displayed in Figure 10, can vary easily by a factor of 10 depending on the assumed parameter set, the thickness of the water shell, and the number of involved MPA molecules. So far, we assumed only a single conductance channel while in category A devices up to four MPA-AuNPs fit into the gap between the electrodes, and a small number of molecules may bridge AuNP and electrode in each connection

dx.doi.org/10.1021/jp405990y | J. Phys. Chem. C XXXX, XXX, XXX–XXX

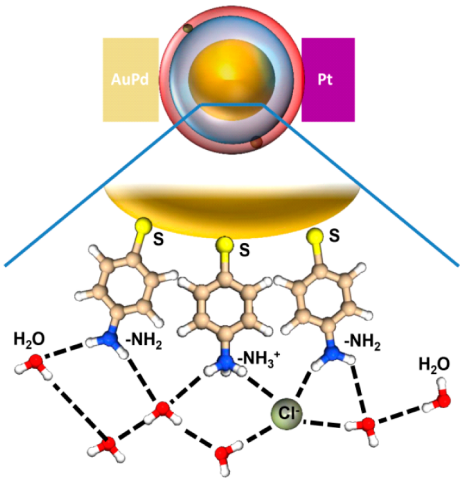

Figure 10. Detailed scheme of the ligand shell surrounding the AuNP, including MPA molecules with partly protonated amine groups, incorporated water molecules and chloride ions.

(for detailed discussion see Supporting Information). However, the small range of experimental values for the conductivity of category A devices suggests well-defined ligand shells with minor variances.

The existence of water molecules loosely bound by hydrogen bonds to the amine groups of the MPA capping layer is in agreement with the noisy I/U curves of category A MPA-AuNP devices (Figure 8), especially regarding the increasing noise corresponding to increasing voltage. The water molecules are expected to move in high electrical fields. Furthermore, the expected rectifier functionality arising from MPA-AuNPs immobilized in heterometallic nanogaps due to different transmission coefficients, i.e., different values of $T_{\mathrm{AuPd\text{-}N}}$ and $T_{\mathrm{Pt-N}}$, or the different binding energies, $BE_{\mathrm{Au-N}} = 0.35$ eV and $BE_{\mathrm{Pt-N}} = 1.42$ eV,[38] will be masked by the water molecules in category A devices, resulting in symmetric I/U curves.

Category B devices, on the other hand, show a largely reduced conductivity (5 orders of magnitude) compared to category A devices. This behavior can be explained only by an increased vacuum gap between MPA-AuNP(s) and one electrode. In consequence, the transport mechanism of these devices is tunneling, and the magnitude of the tunneling current is mainly determined by the size of the vacuum gap. Category B devices can be regarded as asymmetric junctions like molecular junctions in scanning tunneling microscopes (STM), i.e., with a strong coupling to the substrate (electrode1) and a weak coupling to the tip (electrode2). Like in STM configuration the voltage drops mainly over the vacuum gap, and the opening of a conduction channel involving a HOMO or a LUMO of MPA is directly monitored as a peak in the normalized differential conductance (Figure 9b). Transport measurements performed using these devices exhibit clearly the transition from direct to Fowler–Nordheim tunneling (TVS, Figure 9c). The small asymmetry of the I/U measurements obtained from the category B device (Figure 9) is in accordance with the donor character of MPA (i.e., $|\phi_{\mathrm{B,HOMO}}| < |\phi_{\mathrm{B,LUMO}}|$). A possible asymmetry in this kind of devices is based on different activation energies for hole and electron transport, i.e., the difference $|\phi_{\mathrm{B,HOMO}}| - |\phi_{\mathrm{B,LUMO}}|$, and not on differences in contact properties.

CONCLUSION

In conclusion, we have developed a procedure to fabricate asymmetric nanodevices based on dielectrophoretic trapping of molecule capped AuNPs in a heterometallic nanoelectrode gap. This new method allows to predefine the transition coefficients between the molecular anchor groups and the respective nanoelectrodes by a suitable selection of the metals. Especially, anchor group/metal pairs with large differences in transition coefficients are expected to form asymmetric voltage drops across the interfaces and thus show rectifying properties. Using mercaptophenylamine (MPA)-capped AuNPs, two categories of devices were identified based on their respective electronic properties. One device category is characterized by a rather small and widespread conductivity, which is attributed to very small vacuum gaps between the nanoparticle and (at least) one electrode. The asymmetry of I/U characteristics of these devices is determined by the difference in activation energy for electron and hole transport, like in STM experiments. The second device category reveals high and weakly varying conductivities pointing to the formation of asymmetric AuPd-MPA/AuNP/MPA-Pt devices. The expected rectifier functionality arising from these devices due to different transmission coefficients is assumed to be masked by the water molecules incorporated into the ligand shell.

ASSOCIATED CONTENT

Supporting Information

Supplementary data concerning pH-dependent properties of MPA-capped AuNPs and electrical characterization of MPA-AuNPs. This material is available free of charge via the Internet at http://pubs.acs.org.

AUTHOR INFORMATION

Corresponding Author

*Phone ++49 2461 614015; e-mail s.karthaeuser@fz-juelich.de (S.K.).

Notes

The authors declare no competing financial interest.

ACKNOWLEDGMENTS

The authors gratefully acknowledge the help of A. Besmehn, R. Borowski, and S. Trellenkamp. This work was supported by the Excellence Initiative of the German federal and state government and by the Jülich Aachen Research Alliance (JARA).

REFERENCES

(1) Strukov, D.; Likharev, K. Reconfigurable Nano-Crossbar Architectures. In *Nanoelectronics and Information Technology*; Waser, R., Ed.; Wiley-VCH: Weinheim, 2012.

(2) Aviram, A.; Ratner, M. A. Molecular rectifiers. *Chem. Phys. Lett.* **1974**, *29*, 277–283.

(3) Simmons, J. G. Electric Tunnel Effect between Dissimilar Electrodes Separated by a Thin Insulating Film. *J. Appl. Phys.* **1963**, *34*, 2581–2590.

(4) Lüssem, B.; Bjornholm, T. Concepts in Single-Molecule Electronics. In *Nanotechnology*; Waser, R., Ed.; Wiley-VCH: Weinheim, 2008; Vol. 4.

(5) Chen, X.; Yeganeh, S.; Qin, L.; Li, S.; Xue, C.; Braunschweig, A.; Schatz, G.; Ratner, M. A.; Mirkin, C. Chemical Fabrication of Heterometallic Nanogaps for Molecular Transport Junctions. *Nano Lett.* **2009**, *9*, 3974–3979.

(6) Akkerman, H. B.; de Boer, B. Electrical Conduction through Single Molecules and Self-Assembled Monolayers. *J. Phys.: Condens. Matter* **2008**, *20*, 013001 20pp.
(7) Haag, R.; Rampi, M. A.; Holmlin, R. E.; Whitesides, G. M. Electrical Breakdown of Aliphatic and Aromatic Self-Assembled Monolayers Used as Nanometer-Thick Organic Dielectrics. *J. Am. Chem. Soc.* **1999**, *121*, 7895−7906.
(8) Chen, J.; Reed, M. A.; Rawlett, A. M.; Tour, J. M. Large On-Off Ratios and Negative Differential Resistance in a Molecular Electronic Device. *Science* **1999**, *286*, 1550−1552.
(9) Beebe, J. M.; Kushmerick, J. G. Nanoscale Switch Elements from Self-Assembled Monolayers on Silver. *Appl. Phys. Lett.* **2007**, *90*, 083117 3pp.
(10) Chen, X.; Jeon, Y. M.; Jang, J. W.; Qin, L.; Huo, F.; Wie, W.; Mirkin, C. A. On-Wire Lithography-Generated Molecule-Based Transport Junctions: A New Testbed for Molecular Electronics. *J. Am. Chem. Soc.* **2008**, *130*, 8166−8168.
(11) Kashimura, Y.; Nakashima, H.; Furukawa, K.; Torimitsu, K. Fabrication of Nano-Gap Electrodes Using Electroplating Technique. *Thin Solid Films* **2003**, *438*−*439*, 317−321.
(12) Loo, Y.-L.; Lang, D. V.; Rogers, J. A.; Hsu, J. W. P. Electrical Contacts to Molecular Layers by Nanotransfer Printing. *Nano Lett.* **2003**, *3*, 913−917.
(13) Liu, K.; Avouris, Ph.; Bucchignano, J.; Martel, R.; Sun, S.; Michl, J. Simple Fabrication Scheme for Sub-10 nm Electrode Gaps Using Electron-Beam Lithography. *Appl. Phys. Lett.* **2002**, *80*, 865−867.
(14) Kronholz, S.; Karthäuser, S.; van der Hart, A.; Wandlowski, T.; Waser, R. Metallic Nanogaps with Access Windows for Liquid Based Systems. *Microelectron. J.* **2006**, *37*, 591−594.
(15) Manheller, M.; Trellenkamp, S.; Waser, R.; Karthäuser, S. Reliable Fabrication of 3 nm Gaps between Nanoelectrodes by Electron-Beam Lithography. *Nanotechnology* **2012**, *23*, 125302 6pp.
(16) Deshmukh, M.; Prieto, A.; Gu, Q.; Park, H. Fabrication of Asymmetric Electrode Pairs with Nanometer Separation Made of Two Distinct Metals. *Nano Lett.* **2003**, *3*, 1383−1385.
(17) Mészáros, G.; Kronholz, S.; Karthäuser, S.; Mayer, D.; Wandlowski, T. Electrochemical Fabrication and Characterization of Nanocontacts and nm-Sized Gaps. *Appl. Phys. A: Mater. Sci. Process.* **2007**, *87*, 569−575.
(18) Nishino, T.; Negishi, R.; Tanaka, H.; Ogawa, T.; Ishibashi, K. Fabrication of Nanogap Electrodes by the Molecular Lithography Technique. *Jpn. J. Appl. Phys.* **2011**, *50*, 035204 6pp.
(19) Tang, J.; Wang, Y.; Nuckolls, C.; Wind, S. Chemically Responsive Molecular Transistors Fabricated by Self-Aligned Lithography and Chemical Self-assembly. *J. Vac. Sci. Technol., B* **2006**, *24*, 3227−3229.
(20) Beebe, J.; Kim, B.; Gadzuk, J.; Frisbie, C. Transition from Direct Tunneling to Field Emission in Metal-Molecule-Metal Junctions. *Phys. Rev. Lett.* **2006**, *97*, 026801 4pp.
(21) Huisman, E.; Guedon, C.; v. Wees, B.; v. d. Molen, S. J. Interpretation of Transition Voltage Spectroscopy. *Nano Lett.* **2009**, *9*, 3909−3913.
(22) Lennartz, M.; Atodiresei, N.; Caciuc, V.; Karthäuser, S. Identifying Molecular Orbital Energies by Distance-Dependent Transition Voltage Spectroscopy. *J. Phys. Chem. C* **2011**, *115*, 15025−15030.
(23) Kaulen, C.; Homberger, M.; Babajani, N.; Karthäuser, S.; Simon, U. 2013, submitted.
(24) Bellino, M. G.; Calvo, E. J.; Gordillo, G. Adsorption Kinetics of Charged Thiols on Gold Nanoparticles. *Phys. Chem. Chem. Phys.* **2004**, *6*, 424−428.
(25) Pohl, H. *Dielectrophoresis*; Cambridge University Press: Cambridge, UK, 1978.
(26) Barsotti, R.; Vahey, M.; Wartena, R.; Chiang, Y.; Voldman, J.; Stellacci, F. Assembly of Metal Nanoparticles into Nanogaps. *Small* **2007**, *3*, 488−499.
(27) Manheller, M.; Karthäuser, S.; Waser, R.; Blech, K.; Simon, U. Electrical Transport through Single Nanoparticles and Nanoparticle Arrays. *J. Phys. Chem. C* **2012**, *116*, 20657−20665.
(28) Simmons, J. G. Generalized Formula for the Electric Tunnel Effect between Similar Electrodes Separated by a Thin Insulating Film. *J. Appl. Phys.* **1963**, *34*, 1793−1803.
(29) Karthäuser, S. Control of Molecule-Based Transport for Future Molecular Devices. *J. Phys.: Condens. Matter* **2011**, *23*, 013001, 16pp.
(30) Imry, Y.; Landauer, R. Conductance Viewed as Transmission. *Rev. Mod. Phys.* **1999**, *71*, 306−312.
(31) Salomon, A.; Cahen, D.; Lindsay, S.; Tomfohr, J.; Engelkes, V. B.; Frisbie, C. D. Comparison of Electronic Transport Measurements on Organic Molecules. *Adv. Mater.* **2003**, *15*, 1881−1890.
(32) Manheller, M.; Karthäuser, S.; Blech, K.; Simon, U.; Waser, R. Electrical Characterization of Single Biphenyl-Propanethiol Capped 4nm Au Nanoparticles. *Proc. 10th Int. Conf. Nanotechnol. (IEEE-Nano)* **2010**, 919−923.
(33) Lüssem, B.; Müller-Meskamp, L.; Karthäuser, S.; Homberger, M.; Simon, U.; Waser, R. Electrical and Structural Characterization of Biphenylethanethiol SAMs. *J. Phys. Chem. C* **2007**, *111*, 6392−6397.
(34) Chen, F.; Li, X.; Hihath, J.; Huang, Z.; Tao, N. Effect of Anchoring Groups on Single-Molecule Conductance: Comparative Study of Thiol-, Amine-, and Carboxylic-Acid-Terminated Molecules. *J. Am. Chem. Soc.* **2006**, *128*, 15874−15881.
(35) Kiguchi, M.; Miura, S.; Takahashi, T.; Hara, K.; Sawamura, M.; Murakoshi, K. Conductance of Single 1,4-Benzenediamine Molecule Bridging between Au and Pt Electrodes. *J. Phys. Chem. C* **2008**, *112*, 13349−13352.
(36) Blass, P. M.; Zhou, X. L.; White, J. M. Coadsorption and Reaction of Water and Potassium on Silver(III). *J. Phys. Chem.* **1990**, *94*, 3054−3062.
(37) Russot, J. Characterization of Polyamic Acid/Polyimide Films in the Nanometric Thickness Range from Spin-Deposited Polyamic Acid. *Surf. Interface Anal.* **1988**, *11*, 414−420.
(38) Tarazona-Vasquez, F.; Balbuena, P. Complexation of the Lowest Generation Poly(amidoamine)-NH2 Dendrimers with Metal Ions, Metal Atoms, and Cu(II) Hydrates: An ab Initio Study. *J. Phys. Chem. B* **2004**, *108*, 15992−16001.